Bollettino di Geofisica Teorica ed Applicata Vol. 60, n. 1, pp. 97-122; March 2019
DOI 10.4430/bgta0269

Application of magnetic method to define the structural setting controlling the contaminated area of Wadi Bani Malik, east Jeddah, Saudi Arabia

F. Rehman[1,4], M. Abdelazeem[2], M.M. Gobashy[3], H.M. Harbi[4], F. Rehman[5] and H.S.O. Abuelnaga[4]

[1] *Department of Earth Sciences, Quaid-i-Azam University, Islamabad, Pakistan*
[2] *National Research Institute of Astronomy and Geophysics, Cairo, Egypt*
[3] *Department of Geophysics, Faculty of Science, Cairo University, Orman, Giza, Egypt*
[4] *Department of Geophysics, Faculty of Earth Sciences, King Abdulaziz University, Jeddah, Saudi Arabia*
[5] *Department of Earth Sciences, University of Sargodha, Pakistan*

(Received: 12 December 2017; accepted: 24 January 2019)

ABSTRACT The present work deals with ground magnetic investigations of the Wadi Bani Malik area, 40 km from Jeddah city in Saudi Arabia, to delineate the structural settings and demarcate the possible fractures controlling the contaminated flow in the study area. A magnetic survey has been conducted on the up- and downstream areas of the sewage reservoir and filters have been applied to the measured total field, such as reduction to pole (RTP), normalised source strength, tilt angle, and 3D Euler deconvolution to accomplish the goals. Moreover, the Kaczmarz regularisation algorithm was applied to invert RTP data along two selected profiles to magnetic susceptibility depth section to extract magnetic contacts/faults crossing the Wadi. The Wadi is divided into two areas, upstream (Area 2) and downstream (Area 1). The results show that both areas are composed of complex structural trends. In Area 1, magnetic contacts/faults trend mainly in the NE-SW, NNE-SSW and E-W directions, whereas the major trends in Area 2 are NW-SE. The applied filters revealed that in Area 1 the depth to contacts/faults ranges from ~7 m to ~30 m and in Area 2 the depths to contacts/faults are mostly greater than 30 m. Possible subsurface contaminated water flow directions in both areas were deduced from the spatial distribution of these contacts.

Key words: magnetic survey, Bani Malik, contaminant zones, Jeddah, structural setting, NSS, Kaczmarz.

1. Introduction

Wadi Bani Malik, the study area, is located in Makkah quadrangle, which is situated in the central western portion of the Arabian Shield (Fig. 1). Makkah, Jeddah, and Taif are the major metropolitan cities of the central western coast of Saudi Arabia. In the recent past, the central part of the Wadi was used to construct a concrete dam for the dumping of sewage water of Jeddah to avoid the seepage and contamination in the groundwater. In Wadi Bani Malik, crops out the thick sequence of basement rocks, which are cut by different younger magmatic bodies. The rock

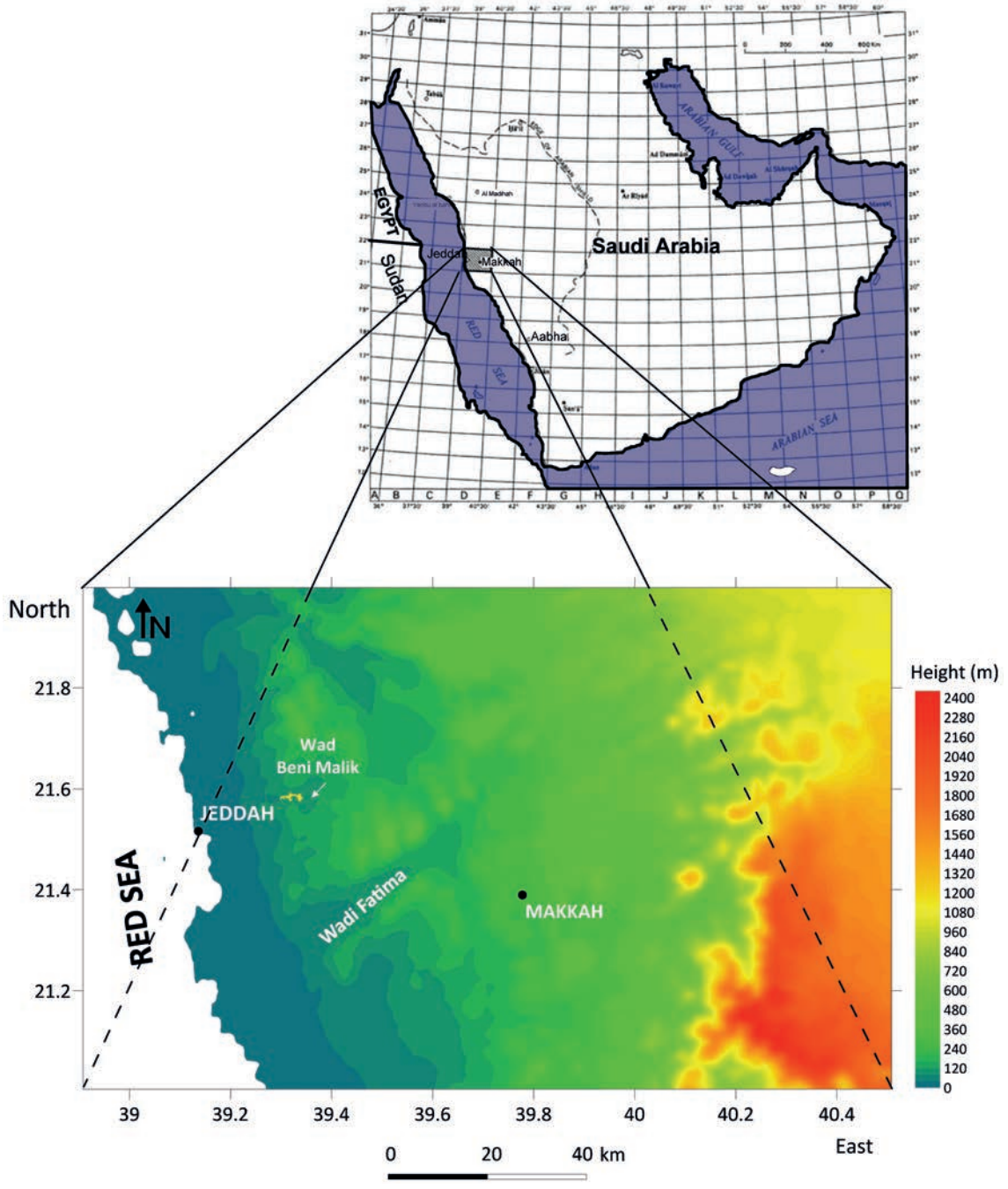

Fig. 1 - Location map of the study area: Makkah quadrangle and Wadi Beni Malik are indicated on a simplified topographic map of the quadrangle (after Moore and Al-Rehaili, 1989).

sequence is covered by the deposits of Quaternary sediments at places (Moore and Al-Rehaili, 1989), and is cut by a complex fault system, which significantly displaced the basement rocks (Al-Garni and Gobashy, 2010).

Geophysical techniques are among the widely used tools to explore the subsurface geology and structural settings for various purposes like petroleum, mineral prospecting, and groundwater

investigations (Ndatuwong and Yadav, 2014; Wang *et al*., 2017). The ground magnetic survey is an accepted technique generally used as a reconnaissance tool to delineate the geology and major structural elements such as magnetic contacts/faults and fractures of buried basement terrains depending upon the varying quantity of magnetic mineral contents in the different rock types (Kearey *et al*., 2013; Loera *et al*., 2015; Soupios and Ntarlagiannis, 2017). Moreover, the magnetic method can also be used to explore the minerals, competency of basement, volcanic bodies and their depths, and archaeological studies (Sarma *et al*., 1999; Grauch *et al*., 2001; Doll *et al*., 2003; Hood, 2007; Howell, 2010; Karavul *et al*., 2010; Kayode *et al*., 2010; Lee *et al*., 2010; Mariita, 2010; Saheel *et al*., 2011; Adagunodo and Sunmonu, 2012). Al-Garni and Gobashy (2010) and Okazaki *et al*. (2011) explored the subsurface topography of basement and subsurface water channels with the help of the magnetic technique. Furthermore, Gobashy and Al-Garni (2008) and Rogers *et al*. (2005) suggested the optimum locations of dams based on these subsurface drainage channels discovered by magnetic analysis.

This research deals with the ground magnetic data of Wadi Bani Malik that are used to delineate the possible magnetic contacts/faults/or fracture system causing the contaminated dam water to leak through into the groundwater aquifer.

2. Study area

Wadi Bani Malik (Fig. 1) is located 40 km away in the east of Jeddah and covers an area of about 302 km^2 (Rehman and Cheema, 2016; Rehman *et al*., 2016). Bani Malik Dam, constructed to dump the sewage water of Jeddah, divides Wadi Bani Malik into two main sectors or areas, namely Area 1, comprising the whole area of the wadi lying downstream of the dam, and Area 2, located along the upstream of the Dam reservoir (Fig. 2).

The dam was essentially constructed to avoid the seepage and contamination of sewage water into the ground water, but unfortunately, it did not achieve the desired goal, and contamination was observed in the groundwater aquifer.

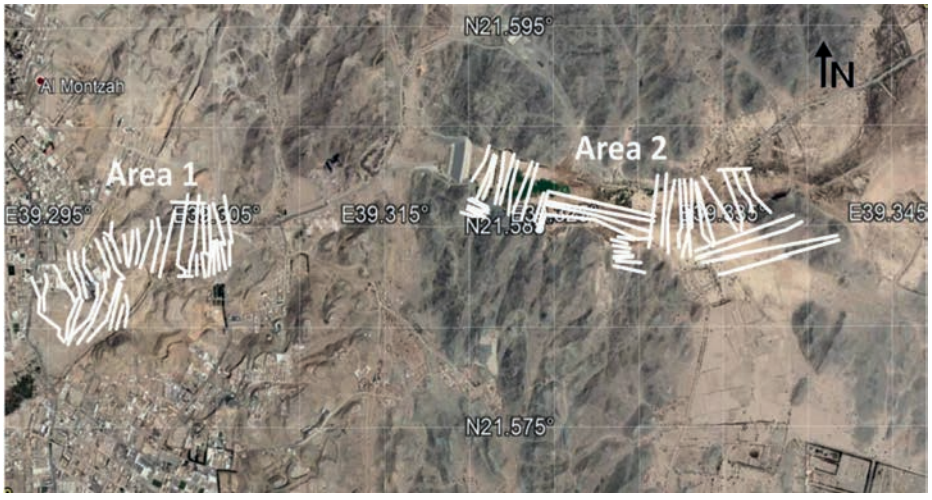

Fig. 2 - Location of surveyed magnetic profiles indicated as solid white lines.

3. Geological setting

At Makkah, the thick sequence of basement rocks mainly crops out, cut by different younger igneous bodies and covered by Quaternary sediments at different places (Moore and Al-Rehaili, 1989; Qari and Sadagah, 2006; Ewea, 2010). Moore and Al-Rehaili (1989) divided the whole sequence into seven main units including the Madrakah formation of Samran group (sm), unassigned metagabbro and gabbro (xgb), Kamil suite comprising of two sub-units Dighbij complex (kddi) and Hafnah complex (khtt), syenogranite of unassigned pluton (gs), mafic dykes and Quaternary deposits (Fig. 3). Stratigraphically, the sequence of Wadi Bani Malik is generally comprised of Madrakah formation, Kamil suite, unassigned metagabbro and gabbro (high magnetic susceptibility), syenogranite and quaternary deposits.

Madrakah formation: it is mainly comprised of volcanic flows of andesite to basaltic composition (which is of high magnetic response due to its high magnetic susceptibility) with subordinate dacite and volcanic clastic of pyroclastic texture. Quartzite and marble are also found at some places.

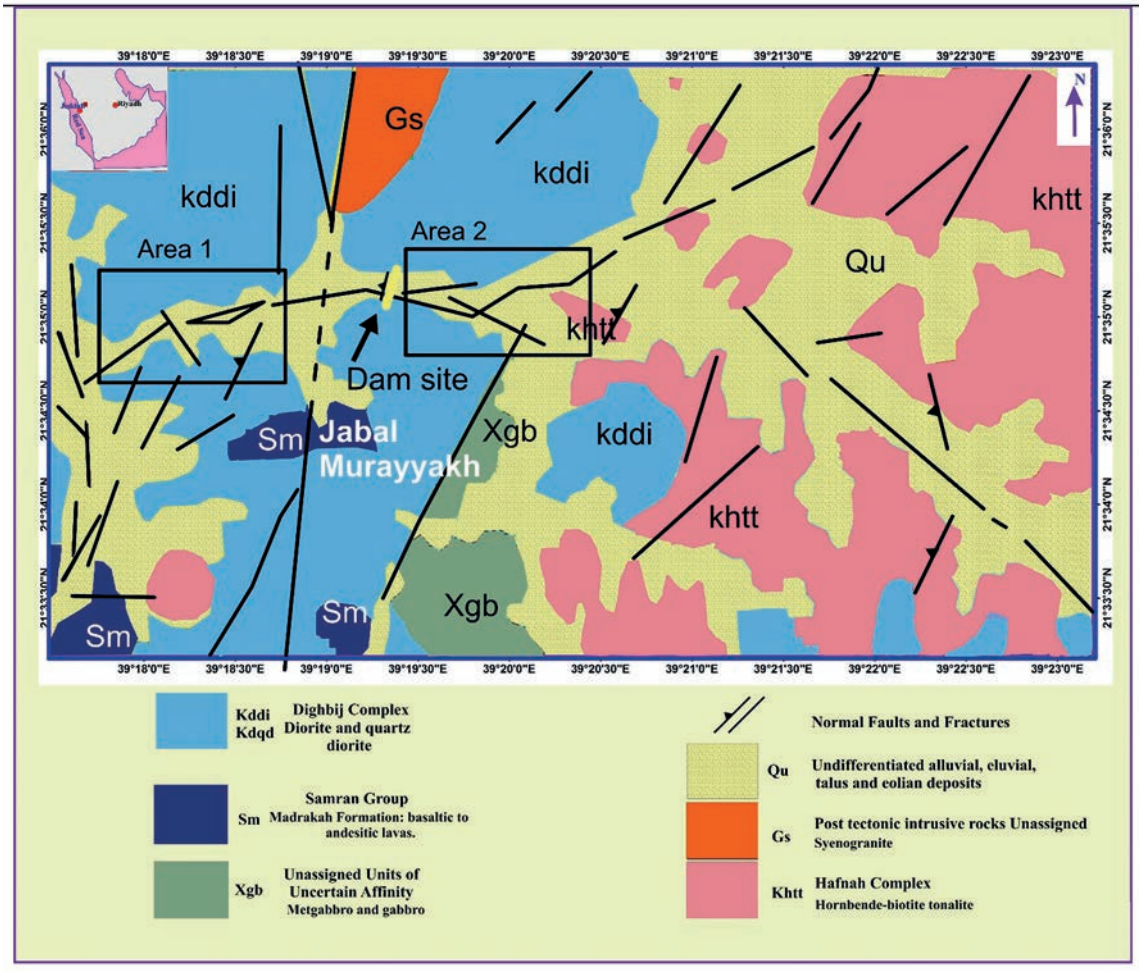

Fig. 3 - Geological map of study area [modified from the original by Moore and Al-Rehaili (1989)].

Syenogranite (low magnetic susceptibility): it is generally pink and fine to medium grained. It occurs in the form of a 15.5-km long body that is intruded north-NE within the Ad-Damm fault zone for 8 km which is 1200 m wide towards its southern end, 120 m wide at Al Hada and 20 m near its north-western termination.

Kamil Suite: it is further divided into two sub-units including Hafnah and Dighbij complexes. Hafnah complex is composed of hornblende tonalite, hornblende-biotite tonalite, quartz monzonite, and trondhjemite. Dighbij complex consists of the diorite, quartz diorite, microdiorite, and quartz monzonite with some xenoliths of unassigned metagabbro and rocks of Samran group widely spread at the south-western margin of the batholith (Moore and Al-Rehaili, 1989; Qari and Sadagah, 2006; Ewea, 2010).

Unassigned metagabbro and gabbro (high magnetic susceptibility): these rocks cover two-thirds of the western part of Makkah quadrangle and are probably the oldest plutonic rocks preserved in the quadrangle. Metagabbro and Gabbro are medium to coarse grained and their colour varies from dark bluish green to dark greenish black. This unit frequently occurs in the form of small pods, sills and large elongated bodies. They generally exhibit a pronounced and well-defined relationship with adjacent rocks.

Quaternary sediments: the deposits of Quaternary sediments occur in the different parts of the study area and cover most of the area of the quadrangle along the coastal plain.

Structurally, the dominant structural trend is NE to NNE and reflects major Precambrian deformation phases (Moore and Al-Rehaily, 1989), and Tertiary faulting. The first deformational phase affected the Zibarah group. This group is an aggregate of the Madiq, Jumum, and Wuhayt formations. It is that part of the Arafat group of Skiba *et al*. (1977) remaining after reclassification of many of its units. It is named after Wadi az Zibarah that crosses the outcrop of the group between the confluence with Wadi ash Shamiyah to the east and AI Khula~ah 17 km to the west. The distinguishing characteristics of the group are the association of quartz-rich schists and metaquartzites with banded amphibolites (the Jumum and Wuhayt formations), a metamorphic grade in the almandine-amphibolite facies, and the presence of structures thought to be related to the earliest tectonic event in the Makkah region. The second phase affected the Samran group, which occurs as rafts within and screens between plutons and as envelopes of country rock around intrusions. The group originally consisted of mafic to felsic lavas and volcaniclastic rocks with subordinate sedimentary rocks. The third affected the Fatima group, which is preserved in NE-trending synclines that rest unconformably on a basement consisting of Samran group rocks, the Rumayda granite, the Sarod tonalite, and the Kamil suite on the north-western side of Wadi Fatima, and to the north of the quadrangle in the Wadi Ghuran-Wadi Fayd area. The most prominent north-easterly-trending structures are the Fatima structural zone and the much younger Ad-Damm fault (the dominant structural feature in the SE of the quadrangle; it extends from the Red Sea coast, in the AI Lith quadrangle, into the adjacent Turabah quadrangle, the fault strikes NE to NNE), both of which have a long history of activity up to the present, as evidenced by microseismic activity (Merghelani and Kinkar, 1983). In the western part of the quadrangle including Wadi Bani Malik, north-NW-trending faults, zones of cataclasis, and dike swarms (Ghumayqah complex) cut Precambrian rocks and Tertiary sedimentary rocks, but not the Tertiary lavas of the Rahat group, and are related to the Red Sea rifting (Moore and Al-Rehaily, 1989).

On the other hand, the north-westerly trending faults are the oldest and have controlled the development of Tertiary depositional troughs (Spencer and Vincent, 1984). They are mostly

normal faults that dip steeply to SW. The fault bounding the Sham trough (occupied by the Hadat ash Sham formation) is probably the oldest, while that separating the Ubhur formation (that underlies the western half of the AI Harra' Lava flow in the NW corner of the Makkah quadrangle and consists mainly of siltstone, green sandy clay, and soft, white bioclastic limestone) from Precambrian rocks is probably the youngest. The continuation of this younger fault under the deposits of the coastal plain is based on an interpretation of gravity and aeromagnetic data by Gettings and Andreasen (1983).

4. Methodology

Magnetic data were obtained using two GEM systems (GSM-19T) proton magnetometer for both stationary (base station fixed unit) and mobile modes (the movable magnetometer). GSM-19T is a microprocessor-based instrument with strong capabilities and large storage memory. It is acquired along nearly N-S trending profiles with a 5-m interval between stations and 20-30 m intervals between profiles depending upon the accessibility of the area. The total number of stations measured in the area is 1337 data points in Area 1 (standard deviation is 32.8 nT) and 2552 data points in Area 2 (standard deviation is 120.27 nT). The data are, then, corrected for diurnal variations with the help of the data acquired by the base station magnetometer, and manually filtered from the micro-pulsation that might exist in the data of artificial or natural origin. After survey levelling, the data are stacked to form the total magnetic maps for both areas 1 and 2.

The international geomagnetic reference field IGRF-12 is calculated for both areas and, then, subtracted to remove the main component of the Earth's geomagnetic field due to the core. The data are, then, reduced to the pole to form the RTP map. Then, RTP map was subjected to tilt angle filter and 3D Euler deconvolution in order to delineate the subsurface structures and the depths to such structures. Fig. 2 shows the location of the surveyed profiles as posted on a Google image.

4.1. Total magnetic intensity map

The total magnetic intensity (TMI) maps (free from IGRF field) of the downstream area (Area 1) and upstream area (Area 2) are shown in Figs. 4a and 4b, respectively. They show significant variations in the magnetic intensity of different sections. Qualitatively, in the downstream area of the dam, the maximum magnetic relative amplitude of ~250 nT (marked as magnetic anomaly C) is recorded along the northern limb of the Wadi and a lowest value of ~ -400 nT (marked as anomaly A) is observed along the southern limb and in small patches of the north-western part of Area 1. There is another zone of relatively magnetic high intensity between these two extremes, marked as anomaly B in the form of an elongated patch lying between the northern and southern limbs and the north-western part of Area 1.

Similarly, the upstream area (Area 2, Fig. 4b) is also characterised by the three zones of magnetic intensities. The maximum magnetic intensity of ~300 nT (marked as anomaly C) is recorded along the north-western limb of the Wadi and the southeast corner, and anomaly A with lowest amplitude of about ~ -500 nT near the southern limb of the Wadi and aligned with the central axis of the Wadi from the western half. The intermediate zone of anomaly B is distributed between the northern and southern limbs.

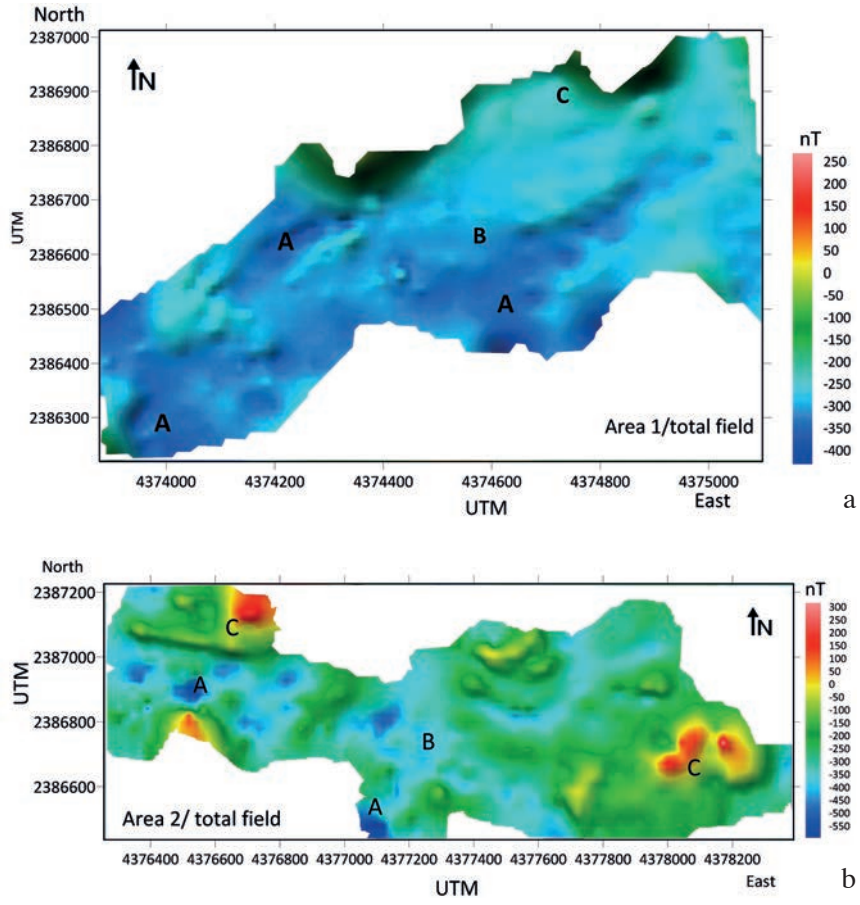

Fig. 4 - Total magnetic intensity map with major anomalies marked A, B, and C: a) Area 1; b) Area 2.

The change in the magnetic anomaly texture is clearly seen in both areas suggesting evidence of disturbed magnetic zones separating regions of different magnetic characters (magnetic susceptibilities) that may be caused by the faults/or contacts and not always related to change in the magnetic properties of the subsurface rocks which is mainly basement in the study area.

4.2. The Reduced-to-Pole (RTP) map

The Reduced-to-Pole (RTP) map was calculated from the total magnetic anomaly maps of regular grids (IGRF free) between the longitudes and latitudes of the studied zones to reduce the dipolar nature of magnetic field and its skewness. The used inclination and declination of the field are (I = 31.130° and D = 3.521°) at the latitude 21° 34' and longitude 39° 19' degrees. These RTP values are later used in the magnetic interpretation and for depth estimation in Wadi Bani Malik, using Euler deconvolution and tilt analysis. Qualitative analyses of the two RTP maps for upstream and downstream areas (Area 2 and Area 1, respectively) show variations in the magnetic characters along the Wadi, with possible identified contacts between zones of different magnetic properties (marked as black lines) from the physical point of view. The trends of major lineaments are shown on the RTP maps (Figs. 5a and 5b). These trends suggest the direction and locations of anticipated linear and curvilinear trends of both studied zones. Moreover, it

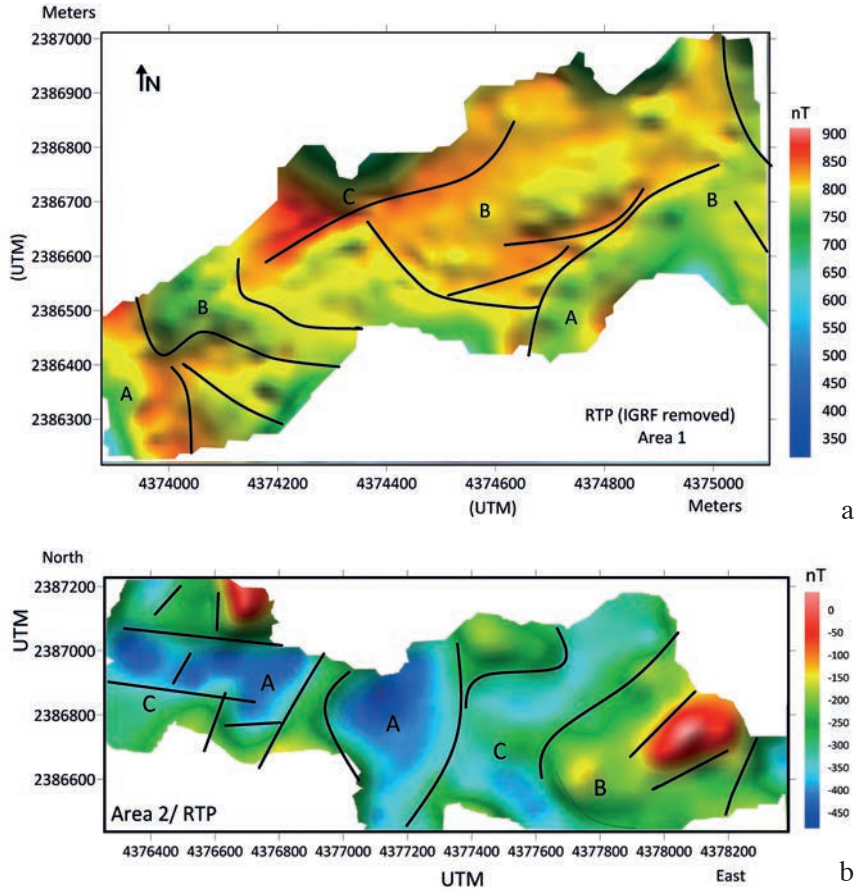

Fig. 5 - RTP magnetic map for the study Area 1 (a) and Area 2 (b).

is possible to discriminate between different zones of high (C), intermediate (B), and low (A) magnetic response.

The RTP map is used to calculate the different directional derivatives. These derivatives (three first order gradients and six second order gradients, i.e. elements of the curvature gradient tensor matrix (CGTM)) are employed to further calculate more complex filters from combinations of these gradients in order to depict the causative source's location, shape, and depth. These include tilt derivative, and 3D Euler deconvolution with unprescribed structural index (SI) in the area under investigation. Linear geologic features, such as faults and contacts, are important since they reflect as lineaments in potential field data. The automated interpretation of potential-field data is aided by evaluating the CGTM (Oruç, 2011) or the gravity gradient tensor (GGT) (Paoletti *et al*., 2016) and beneficial results are obtained. There are considerable advantages in using such gradients in interpretation, especially if the objective is to study magnetic anomalies produced by magnetisation contrasts in the shallow subsurface (e.g. Wadi deposits and its magnetic inhomogeneity). This is because gradient (especially second derivatives) enhances short wavelength signals related to long wavelength signals. The power spectrum of a magnetic gradient measurement along any line is identical to the power spectrum of the field measured multiplied by the wavenumber along the same line. This means that signals from shallow sources are greatly enhanced with respect to the deep ones.

4.3. Normalised source strength (NSS) anomaly and the remnant content

A major source of uncertainty and ambiguity in magnetic survey data interpretation lies in the fact that the physical property contrast that produces the observed magnetic anomalies is a vector quantity and the magnetisation may have almost any direction. In the absence of unrestrained information about source magnetisation, magnetic inversion is carried out on the assumption that the source magnetisation is parallel to the local geomagnetic field (Beiki *et al*., 2012). However, if the source magnetisation direction shifts from the present magnetic field direction, due to possible strong anisotropy or remnant magnetisation, models that fit the data may be erroneous. Most common transforms (e.g. RTP and pseudogravity field maps) suffer from certain limitations: the RTP, for example, needs information about the inclination and declination of both the source magnetisation vector and the geomagnetic field. Since it is common to have significant remnant magnetisation of the source, the source magnetisation vector direction may be unknown. In addition, the calculation of the RTP is unstable at low magnetic latitudes <15 degrees (Silva, 1986).

For that reason, we calculated the normalised source strength transformed anomaly map and the Konigsberger ratio to check the extent of the inherent content of residue in the observed TMI data. Figs. 6a and 6b show the resulting field after removing the remnant magnetisation effect using the NSS transformation on the TMI map free from the IGRF component. The NSS transformed map derived from the magnetic gradient tensor (MGT) is independent of magnetisation direction for a variety of sources, and is only partly dependent on magnetisation direction in general. Moreover, because it satisfies Euler's homogeneity equation (Beiki *et al*., 2012), it can be used to locate magnetic sources.

Briefly, the magnetic field B from a magnetisation distribution M, in volume V, can be written as (Blakely, 1995):

$$B(r) = -C_m \nabla_{r_0} \Phi(r) = -C_m \nabla_{r_0} \int_V M(r_0).\nabla_{r_0} \frac{1}{|r - r_0|}\, dv, \qquad (1)$$

where Φ is magnetic scalar potential, r and r_o are the position vectors of the observation and integration points, respectively, and $C_m = 10^{-7}$ Henry/m in SI units. The magnetic gradient tensor Γ then is (Clark, 2009)

$$\Gamma = -C_m \begin{bmatrix} \frac{\partial^2 \Phi}{\partial x^2} & \frac{\partial^2 \Phi}{\partial x \partial y} & \frac{\partial^2 \Phi}{\partial x \partial z} \\ \frac{\partial^2 \Phi}{\partial x \partial y} & \frac{\partial^2 \Phi}{\partial y^2} & \frac{\partial^2 \Phi}{\partial y \partial z} \\ \frac{\partial^2 \Phi}{\partial x \partial z} & \frac{\partial^2 \Phi}{\partial y \partial z} & \frac{\partial^2 \Phi}{\partial z^2} \end{bmatrix} = \begin{bmatrix} B_{xx} & B_{xy} & B_{xz} \\ B_{xy} & B_{yy} & B_{yz} \\ B_{xz} & B_{yz} & B_{zz} \end{bmatrix}, \qquad (2)$$

Γ can be diagonalised as

$$\Gamma = V^T \Lambda V; \qquad (3)$$

where $V = [V1\ V2\ V3]$ and $\Lambda = \begin{bmatrix} \lambda_1 & 0 & 0 \\ 0 & \lambda_2 & 0 \\ 0 & 0 & \lambda_3 \end{bmatrix}$ contains eigenvalues and eigenvectors, respectively.

In terms of the eigenvalues of the gradient tensor: $I_1 = \lambda_1\lambda_2 + \lambda_1\lambda_3 + \lambda_2\lambda_3$ and $I_2 = \lambda_1\lambda_2\lambda_3$ ($\lambda_1 \geq \lambda_2 \geq \lambda_3$) which satisfies the cubic characteristic equation:

$$\lambda_i^3 + I_1\lambda_i - I_2 = 0, \qquad i = 1, 2, and\ 3. \tag{4}$$

The normalised magnetic moment μ_m (NSS) and the angle between displacement vector and magnetic moment vector (Φ) are given by (Beiki *et al*., 2012):

$$\mu_m = \sqrt{-\lambda_2^2 - \lambda_1\lambda_3} \tag{5}$$

and

$$\Phi = cos^{-1}\left(\frac{\lambda_2}{\mu}\right);\ 0 \leq \Phi \leq 180^o, \tag{6}$$

Figs. 6a and 6b show that both maps contain the general magnetic texture as the RTP map. More fine detailed and resolved anomalies can be observed and detected. The calculated Konigsberger ratio (Q) for both areas using Helbig (1963) are 0.99724 for Area 2, and 1.00453 for Area 1.

Helbig (1963) proposed that it is possible to calculate the resultant magnetisation direction of a remnant-magnetised body without having to create a model, i.e. remotely. While the resultant magnetisation does not allow us to calculate the remnant magnetisation vector or Konigsberger ratio (Q), it does provide a first order indicator of remnant content. The results show that Q is close to 1 in both areas, so the remnant content is acceptable and the RTP can still be used for further magnetic inversion.

4.4. Horizontal and total gradients

The horizontal gradient $\boldsymbol{h}(x, y)$, and the total gradient $\boldsymbol{a}(x, y)$ (or analytic signal amplitude, **ASA**) are the frequently used filters to interpret magnetic maps. The following simple formulae are used to compute the horizontal gradient ($\boldsymbol{h}$) and total gradient ($\boldsymbol{a}$) in time domain, respectively:

$$\begin{cases} \boldsymbol{h}(x,y) = [(d^2T/dx^2)^2 + (d^2T/dy^2)^2]^{1/2}, \text{ and} \\ \boldsymbol{a}(x,y) = [d^2T/dx^2 + d^2T/dy2 + d^2T/dz^2]^{1/2}. \end{cases} \tag{7}$$

where, T is the measured total magnetic field reduced to pole and x, y, and z are the three Cartesian coordinates in the north, east, and vertical direction. The results of these filters when used in the appropriate way will indicate significant lateral variation in the magnetisation boundaries. The horizontal gradient filter is recommended for edge detection only when a pseudogravity transformation of the observed TMI can be conducted with confidence, taking into account that the pseudogravity transformation involves a magnetic RTP calculation (Li, 2006). RTP suffers from two problems: at low magnetic latitudes, RTP is extremely unstable and the remnant magnetisation is usually unknown [Cordell and Grauch (1985)]. Because of this latter reason, we will not use this filter for edge detection and only the total gradient filter will be used.

The total gradient filter ($\boldsymbol{a}$) infers prominent contacts or boundaries between different magnetic bodies with clear linear and curvilinear trends overlapping the maximum magnitude of $\boldsymbol{a}$. The use of this filter is recommended, for edge detection, only in the absence of the knowledge of the ambient and particularly remnant field parameters (Li, 2006). In addition, there are two essential

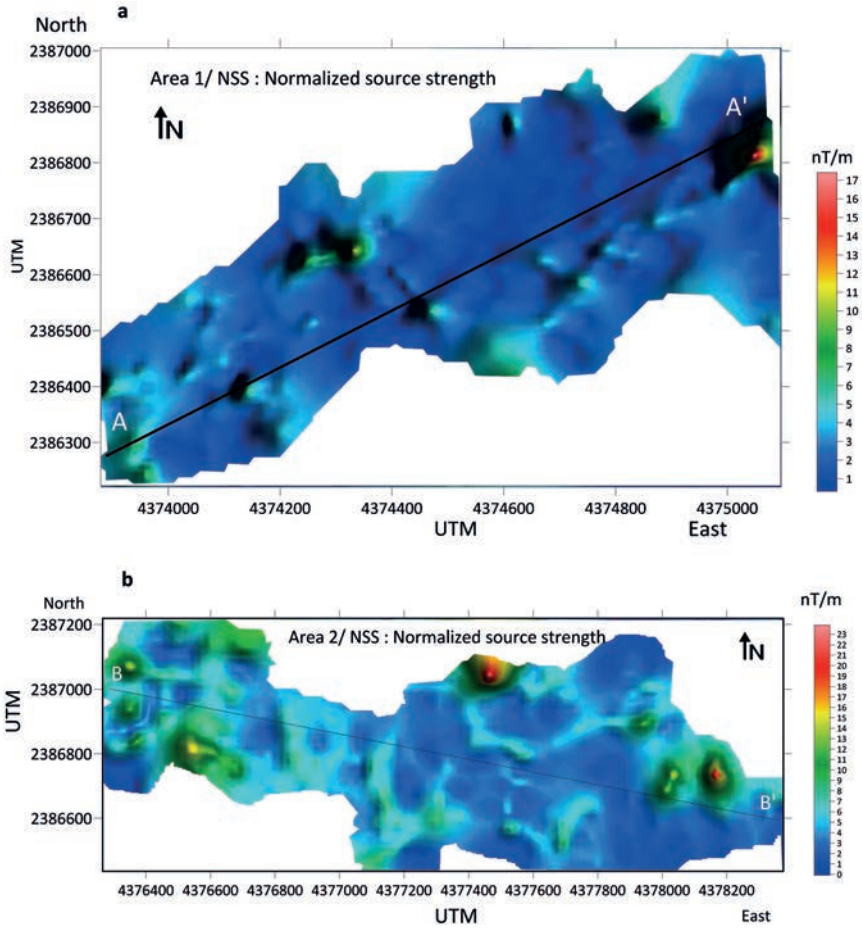

Fig. 6 - Normalised source strength anomaly maps for Area 1 (a) and Area 2 (b).

conditions to apply the total gradient: first, to be sure that the expected finite dipping step model is shallow and second, it is defined only for observations on a horizontal surface (Roest *et al*., 1992). The above conditions are considered when applying the filter on Wadi Bani Malik data, where most of the expected contacts are shallow (<70 m for Area 1, and <30 m for Area 2). This is confirmed from the analyses of the 3D Euler results as in section 4.5, and the Wadi is inherently a relatively flat land.

The trends inferred by ***a*** (Fig. 7) are NE-SW, NNE and SSW. These trends show a perpendicular relationship with the Najd fault system, which is a major transcurrent (strike-slip) fault system of Proterozoic age in the Arabian Shield. Some of these detected trends are on the borders of the area, and, because they are relatively shallow, they can easily be detected by total gradient filter. These trends are also present in the horizontal gradient and total gradient maps of upstream Area 2 (Fig. 8). However, the total gradient map shows completely different NW-SE trends. Geologically, these opposite trending (NW-SE) faults indicate their association with the epeirogenic movements occurring during the Ash Shabah orogenic phase. The eperiogenic movements of this phase cut the Precambrian basement into four major NW aligned blocks in the northern part of the Arabian Shield with the help of wide left lateral fault system, the Najd fault system (NFS).

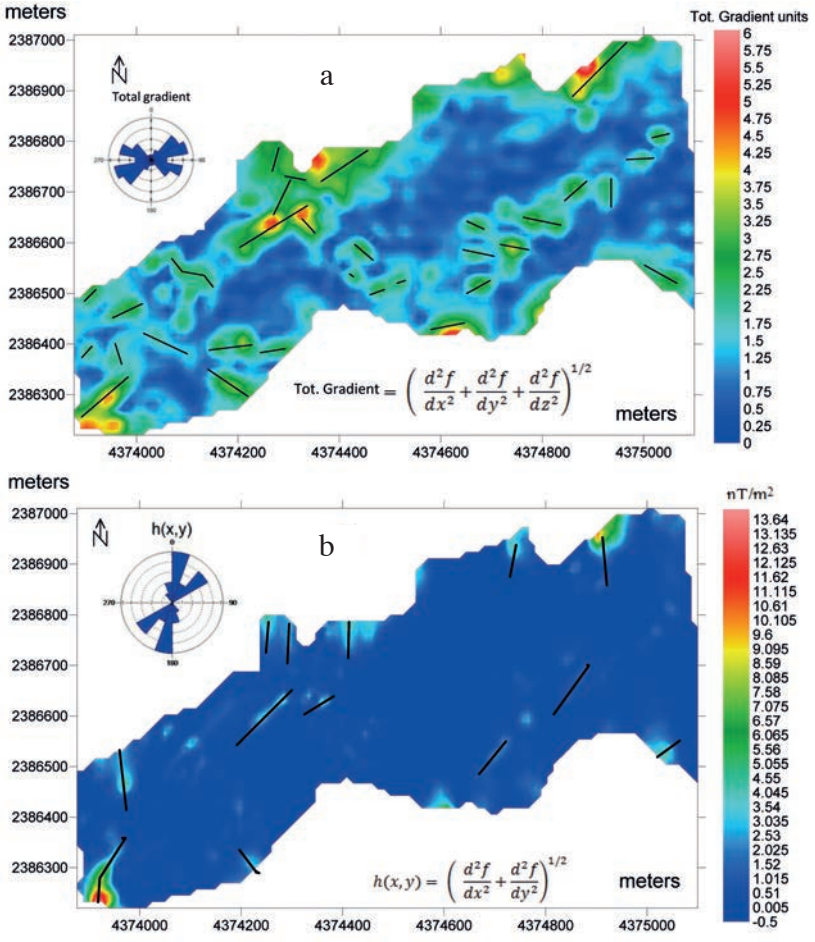

Fig. 7 - RTP map of study Area 1 showing preliminary edge detection and the dominant NE-SW, NNE-SSW trends: a) total gradient; b) horizontal gradient.

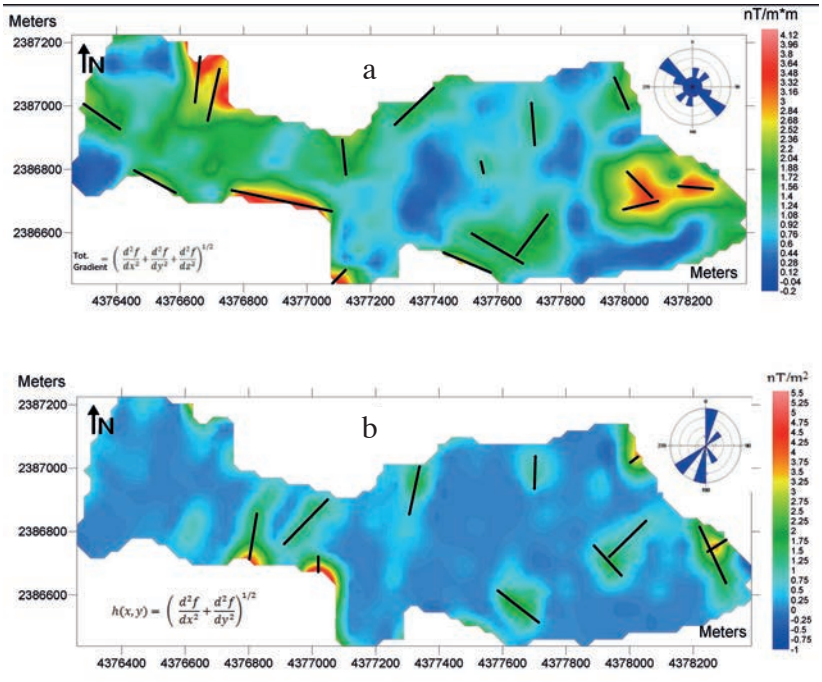

Fig. 8 - RTP map of Area 2 showing preliminary edge detection and the dominant NE-SW, NNE-SSW, and NW-SE trends: a) total gradient; b) horizontal gradient.

4.5. 3D Euler deconvolution and automatic structural index identification

The 3D Euler deconvolution is a commonly used technique to estimate the causative source depths. It is formally applied to estimate the coordinates and constant background for tentative SI values. Gerovska and Araúzo-Bravo (2003) revised the method of Stavrev (1997) by using large amounts of data and presented a completely automatic method to compute the source depth with automatic determination of the SIs. Briefly, the technique is mainly based on the differential similarity transformation (DST). A similarity transformation in relation to a coordinates centre $O'(a,b,c)$ is a homotopic transformation with a scaling parameter $n>0$, represented by the equations (Stavrev, 1997):

$$\begin{aligned} x' &= a + (x - a)n, \\ y' &= b + (x - b)n, \\ c' &= c + (x - c)n. \end{aligned} \tag{8}$$

A differential similarity transformation also represents the difference between the original field and the field after a similarity transformation with respect to a certain central point of similarity (CPS) O' and a coefficient of similarity n = -N. The DSTs operator S^{-N} [.] O', applied on a general function $f(p)$, is defined in Stavrev (1997) as:

$$S^{-N}[f(P)]O' = -N f(P) - RO'P \nabla P f(P) \tag{9}$$

where P is the observation point, $RO'P$ is a vector from a point O' to the point P, and $\nabla_p f(p)$ is the gradient of (f) with respect to P. In the case of a magnetic or gravity anomaly A, the distribution and amplitude of $S^{-N}[A]O'$, are directly related to the position of the CPS O' with respect to the source of A.

The algorithm, presented by Stavrev (1997), is based on the fact that: when the CPS coincides with the source singular point, the $S^{-N}[A]_{O'}$, of the anomaly field becomes a zero at all observation points. The DST operator $S^{-N}[.]_{O'}$ is linear, and therefore $S^{-N}[A + B]_{O'} = S^{-N}[A]_{O'} + S^{-N}[B]_{O'}$. When the background B is linear, $S^{-N}[F]_{O'}$ is linear, and then $S^{-N}[F]_{O'}$ of the measured field $F(P)$ also becomes linear.

In this work, techniques devised by Stavrev (1997) and Gerovska and Araúzo-Bravo (2003) are employed to interpret the magnetic anomalies and source depths in the Bani Malik region. In 3D Euler data analysis, the two-stage clustering method has frequently been used on the data to infer the horizontal locations and to compute the depths of causative sources (Gerovska and Araúzo-Bravo, 2003).

The 3D Euler deconvolution analysis is applied to RTP magnetic maps of both parts of Wadi Bani Malik. A window of 8×16 grid data points is selected in the north (y) and east (x) directions, respectively, with grid spacing of 0.55 km in both directions. The already computed partial derivatives are utilised and the problem of edge effects is overcome by extending north and east grids to 10% with half cosine function before the calculation of the vertical derivative. Finally, the extended area of each obtained grid was reversed into the original size of initial grid. The survey height of 0 m is used for this purpose. Figs. 9 and 10 show the results of these techniques for downstream Area 1 and upstream Area 2. Figs. 9a and 9b present the clusters of horizontal projections of the downstream Area 1 and upstream Area 2, respectively, which was constructed

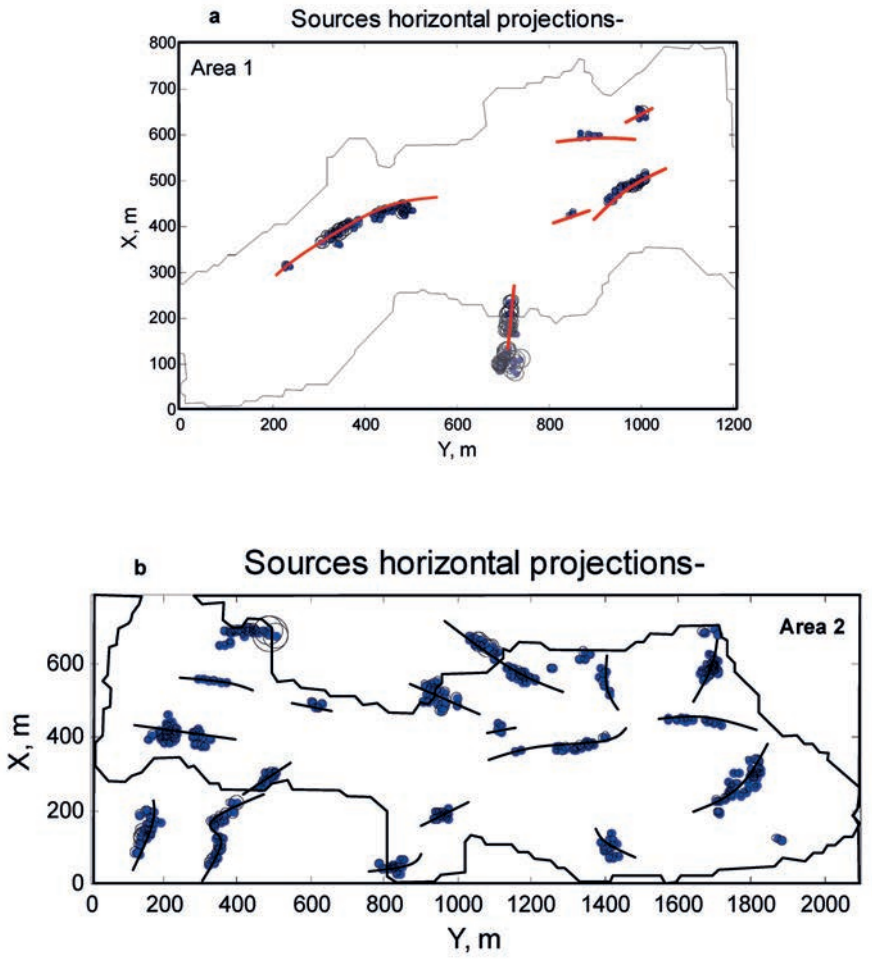

Fig. 9 - 3D Euler deconvolution analysis, sources horizontal projections with linear trends indicated: a) Area 1; b) Area 2.

Table 1 - Statistical analysis of the clusters of Area 1 (second stage).

Cluster	NumPoi	Xavr	Xcon	Yavr	Ycon	Zavr	Zcon	Navr	Ncon
1	87	411.93	65.18	402.52	142.43	15.41	13.89	0.706	1.084
2	69	143.30	89.43	707.46	21.895	28.96	16.12	0.300	0.520
3	38	484.09	43.59	965.59	85.592	16.66	10.44	0.416	0.737
4	6	599.54	9.387	885.53	42.102	7.44	7.332	0.203	0.538
5	9	648.02	18.15	998.83	11.249	12.30	16.79	1.078	1.402

NumPoi: Number of points
Xave: Average x value
Xcon: Confidence interval for variable X
Yave: Average Y value
Ycon: Confidence interval for variable Y
Zave: Average z value
Zcon: Confidence interval for variable Z
Nave: Average estimated structural indices for each cluster
Ncon: Confidence interval for estimated structural indices N

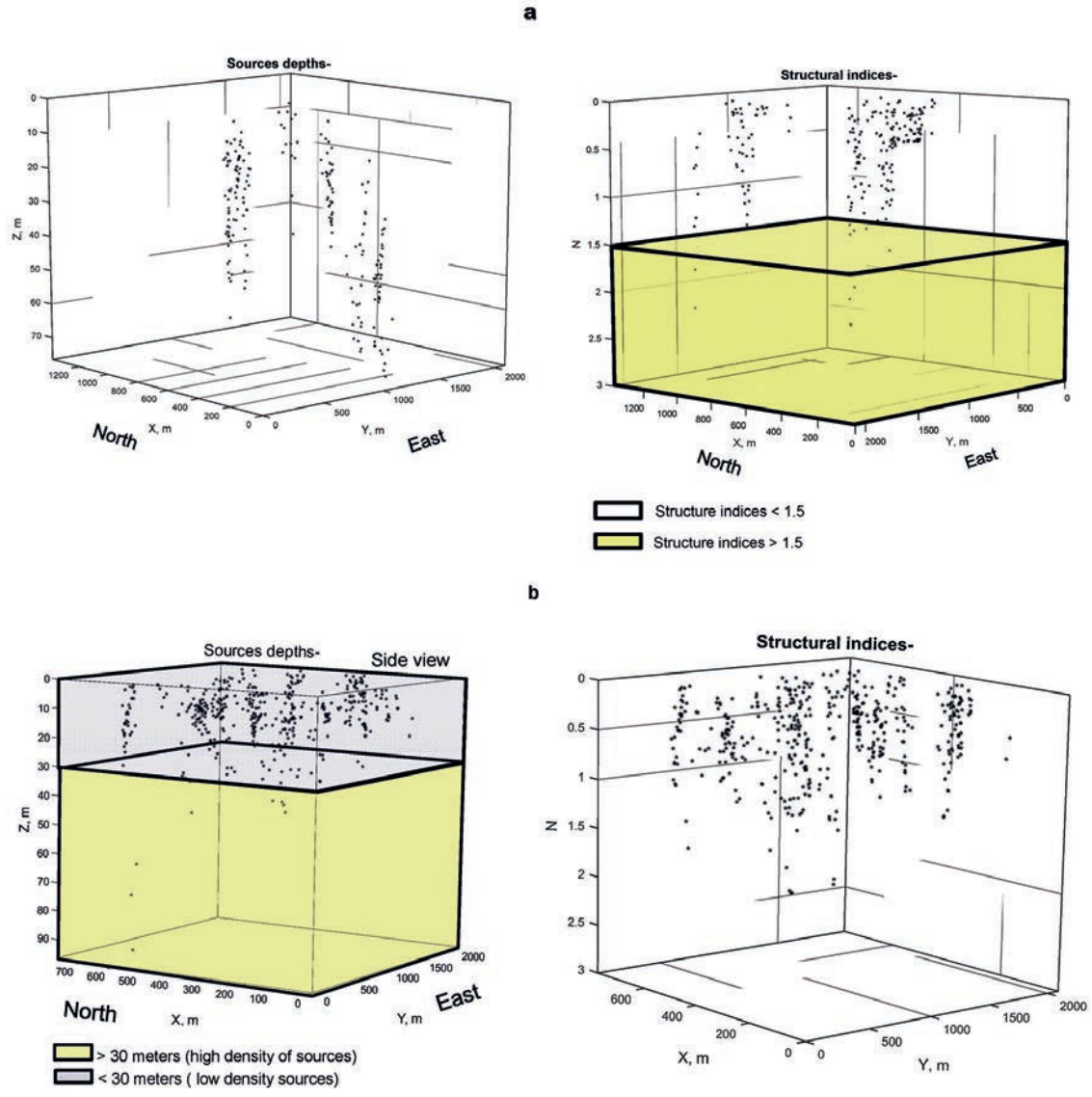

Fig. 10 - A perspective view for the structural indices and source depths for Area 1 (a) and for Area 2 (b).

by applying the second cluster stage and primary statistics solution with fusion clusters algorithm (Gerovska and Araúzo-Bravo, 2003; Azeem *et al*., 2014).

As for Area 1, statistical analysis of clusters is presented in Tables 1 and 2. The cautious assessment of the data indicates that two clusters (4 and 5) represent very shallow depth, whereas three clusters (1, 2, 3) represent relatively deep sources.

As for the upstream Area 2, the results show that the NW-SE is the common trend in this area. In Table 3, clusters after statistical analyses for Area 2 are tabulated. The N_{avr} values show that most of the structural index N is smaller than 1 (N<1) for deduced source anomalies, which suggest a contact/fault model structure. In Table 4, after second stage clustering, some accepted solution coordinates are presented.

Table 2 - Example of some accepted solution coordinates after second stage clustering for Area 1.

serial	X0	Y0	Z0	Structural index SI
1	311.97515	226.72936	7.4741368	0.07
2	319.08392	227.85099	7.8271081	0.11
3	317.60624	231.68507	13.629788	0.40
4	314.10935	237.37137	8.7563495	0.04
5	366.06949	304.27873	25.46384	0.31
6	381.649	316.33473	20.733693	0.06
7	366.82121	308.71105	26.971404	0.48
8	383.00814	322.59678	20.447536	0.29
9	377.8081	322.44348	22.631993	0.47
10	386.30513	330.90656	19.628694	0.44
11	382.61601	330.80926	21.347164	0.50
12	387.78639	337.1361	17.570219	0.46
13	397.74881	345.47631	7.8463403	0.08
14	382.15516	330.77842	21.254258	0.53
15	387.07667	338.46028	17.213669	0.47
16	398.91138	349.79869	8.1255783	0.16
17	371.84316	324.77692	8.8554224	0.05
18	385.06935	333.32761	18.600675	0.48
19	390.82547	341.59767	16.714934	0.47
20	400.24607	351.1834	9.2794032	0.23
21	412.00952	361.78241	6.1723118	0.02
22	375.10271	329.14851	13.819177	0.45
23	389.3347	338.11382	21.22143	0.73
24	399.78603	351.64881	20.838705	0.72
25	405.26039	358.54044	15.554959	0.49
26	412.3048	364.56519	9.9979741	0.18
27	363.2182	338.77104	10.220017	0.34
28	383.14821	340.62562	22.055034	0.99
29	391.81068	344.09292	28.389101	1.15
30	399.45471	354.66913	25.71418	0.99

Figs. 10a and 10b show a perspective view for the SIs and source depths for Area 1 (a) and for Area 2 (b). Solutions for Area 1 show a tendency of SIs to be less than 0.5 and close to 0, indicating magnetic contacts and possible sheet/sill like bodies. The depths to these sources are shallow and concentrate between 10 and 70 m. Solutions for Area 2 show concentration of magnetic source depth below 30 m, while the SIs range between 0 and 1, indicating a structure between a contact (SI = 0) and a fault (small step) (SI = 1) (FitzGerald *et al*., 2004). In general, vertical contacts, or faults, (SI ~0) are still the common structure.

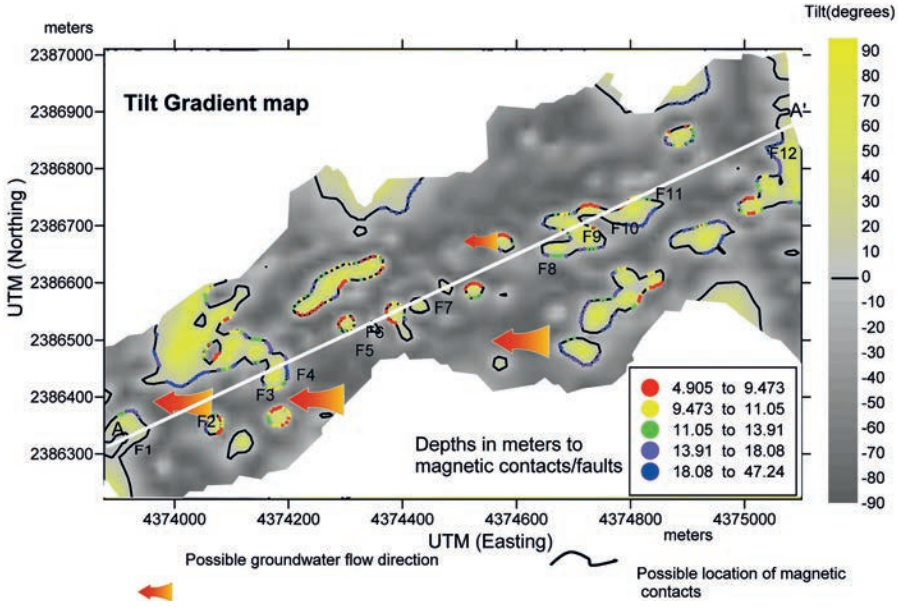

Fig. 11 - Area 1, tilt gradient map showing location of possible edges and magnetic contacts. The possible direction of groundwater flow is also shown by arrows.

4.6. Tilt Depth Method

Salem *et al*. (2008) devised the Tilt Depth Method to identify the locations of faults and vertical contacts. In this study, the RTP magnetic map is used to calculate the tilt depths in both zones, Area 1 (Fig. 11) and Area 2 (Fig. 12). The tilt angle method spontaneously demarcates magnetic sources depth with no remnant magnetisation assumption (Salem *et al*., 2007; Azeem *et al*., 2014). In this technique, assuming a vertical contact model, the value of the tilt angle θ (above the edges of the

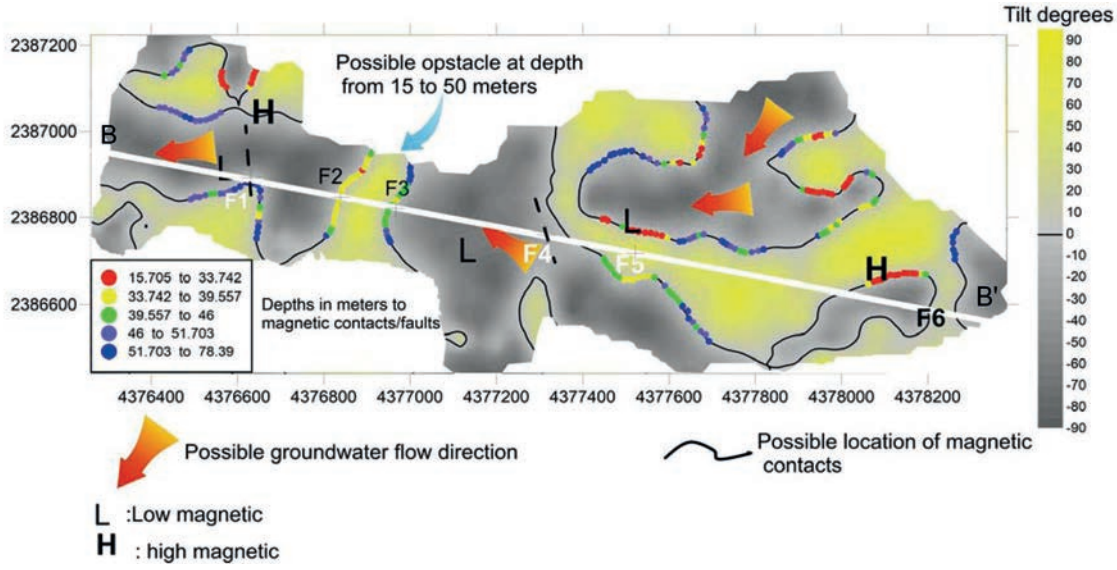

Fig. 12 - Area 2, tilt gradient map showing location of possible edges and magnetic contacts. The possible direction of groundwater flow is also shown by arrows.

Table 3 - Statistical analysis of the clusters of Area 2 (second stage).

Cluster	NumPoi	Xavr	Xcon	Yavr	Ycon	Zavr	Zcon	Navr	Ncon
1	27	149.10	64.371	151.61	33.22	20.86	19.79	0.78	0.96
2	89	525.42	265.03	312.46	196.88	13.39	27.69	0.50	0.61
3	46	183.32	170.08	390.04	131.66	14.43	15.75	0.60	0.71
4	7	489.26	15.61	615.80	23.12	10.49	10.88	0.23	0.35
5	18	49.591	20.70	826.08	35.82	11.97	14.82	0.38	0.55
6	159	542.87	174.49	1340.70	542.07	14.37	18.31	0.44	0.66
7	18	192.65	18.24	956.86	27.47	10.58	6.74	0.37	0.51
8	16	102.01	40.29	1414.70	27.91	8.59	7.88	0.26	0.38
9	64	294.21	141.15	1769.33	98.18	8.38	11.46	0.42	0.70

NumPoi: Number of points
Xave: Average x value
Xcon: Confidence interval for variable X
Yave: Average Y value
Ycon: Confidence interval for variable Y
Zave: Average z value
Zcon: Confidence interval for variable Z
Nave: Average estimated structural indices for each cluster
Ncon: Confidence interval for estimated structural indices N

contact is 0° ($h = 0$) where h is the horizontal coordinate and z_c is the depth to the top, and is equal to 45° when $h = z_c$, and –45° when $h = -z_c$. This suggests that contours of the magnetic tilt angle can identify both the location ($\theta = 0°$) and depth (half the physical distance between ±45° contours) of contact-like structures. In other words, the zero-contour line represents the location or surface projection of magnetic edges resembling the vertical contacts in the study area. Some of these edges present parts of well-known surface faults (deduced from surface geology and Landsat images) and the rest correspond to subsurface sources. The calculated depth to the edges ranges between 4.9 to 47.24 m for Area 1 (Fig. 11) and between 15 and 78 m for Area 2 (Fig. 12). It is evident that the spatial distribution of contacts, resulting from the tilt gradient analysis, can play a critical role in the flow of the groundwater. Moreover, the contaminated water behind the dam is also and most probably affected by these shallow contacts/faults and a possible water exchange between this contaminated water and the natural aquifer may occur along these contacts or weak zones.

4.7. Kaczmarz regularised magnetic tomography

As for quantitative confirmation of the above conclusion, we carried out 2D magnetic inversion (magnetic tomography) along two profiles crossing the depicted faults of Wadi Bani Malik. The technique proposed by Abdelazeem and Gobashy (2016) has been applied using Kaczmarz (1937) regularisation strategy.

To proceed with the inversion procedure, the subsurface model domain is subdivided into two-dimensional prisms of equal sides and each prism is extended to infinity in the third direction perpendicular to the plane. Each prism has an unknown magnetic susceptibility. The problem can be expressed as:

$$\min_x (Ax - b)^T W (Ax - b) \tag{10}$$

Table 4 - Example of some accepted solution coordinates after second stage clustering for Area 2.

serial	X0	Y0	Z0	Structural index SI
1	88.883832	122.9977	27.779844	0.68
2	111.70241	132.66343	25.841705	1.11
3	126.29077	137.09301	39.999791	1.72
4	131.59461	138.85759	37.602219	1.72
5	138.06437	141.01957	36.445346	1.70
6	149.52506	140.41326	32.62764	1.49
7	192.00648	134.43551	25.150002	0.79
8	395.67607	155.60976	8.4583827	0.37
9	408.85003	167.38663	13.921519	0.54
10	85.989862	131.44425	25.396807	0.52
11	110.04616	134.75736	17.125348	0.80
12	130.82536	137.17234	17.348687	0.98
13	144.12913	141.17622	14.104582	0.91
14	151.75461	149.69891	17.998774	0.9
15	165.95005	154.13295	20.242627	0.87
16	197.70301	150.08391	29.633912	0.66
17	388.1512	201.67814	9.7947266	0.45
18	397.39313	193.06161	6.4625107	0.32
19	401.00433	190.28336	6.4273919	0.18
20	404.61351	191.32901	7.4417394	0.19
21	412.04563	190.57691	7.2467511	0.37
22	421.39706	186.95514	4.9400326	0.08
23	127.55088	152.03353	14.335567	0.59
24	136.07833	157.58325	21.072172	0.82
25	148.98355	158.72357	19.959586	0.84
26	166.42547	161.84679	22.967964	0.93
27	182.91633	163.48588	26.746067	0.85
28	202.32626	152.84945	24.049183	0.43
29	393.41373	209.80362	13.927418	0.75
30	403.94435	201.23627	13.111391	0.64

A is the kernel matrix, which expresses the geometrical relation between each prism and each measuring point, *x* is the vector of unknown magnetic susceptibility of prisms, *b* is the vector of measured magnetic field and *W* is the depth weighting diagonal matrix. The above form is a discrete form of ill-conditioned linear algebraic system that can be solved using the Tikhonov regularisation literately (Abdelazeem, 2013). The condition number of the kernel matrix A (the condition No. = 8.3525e + 18 in Area 1 and 2.9785e + 19 in Area 2) proves the above problem is ill-posed. The Euler equation (regularised normal equations) is given as:

$$(A^T A + \alpha^2 I)x_\alpha = A^T b \tag{11}$$

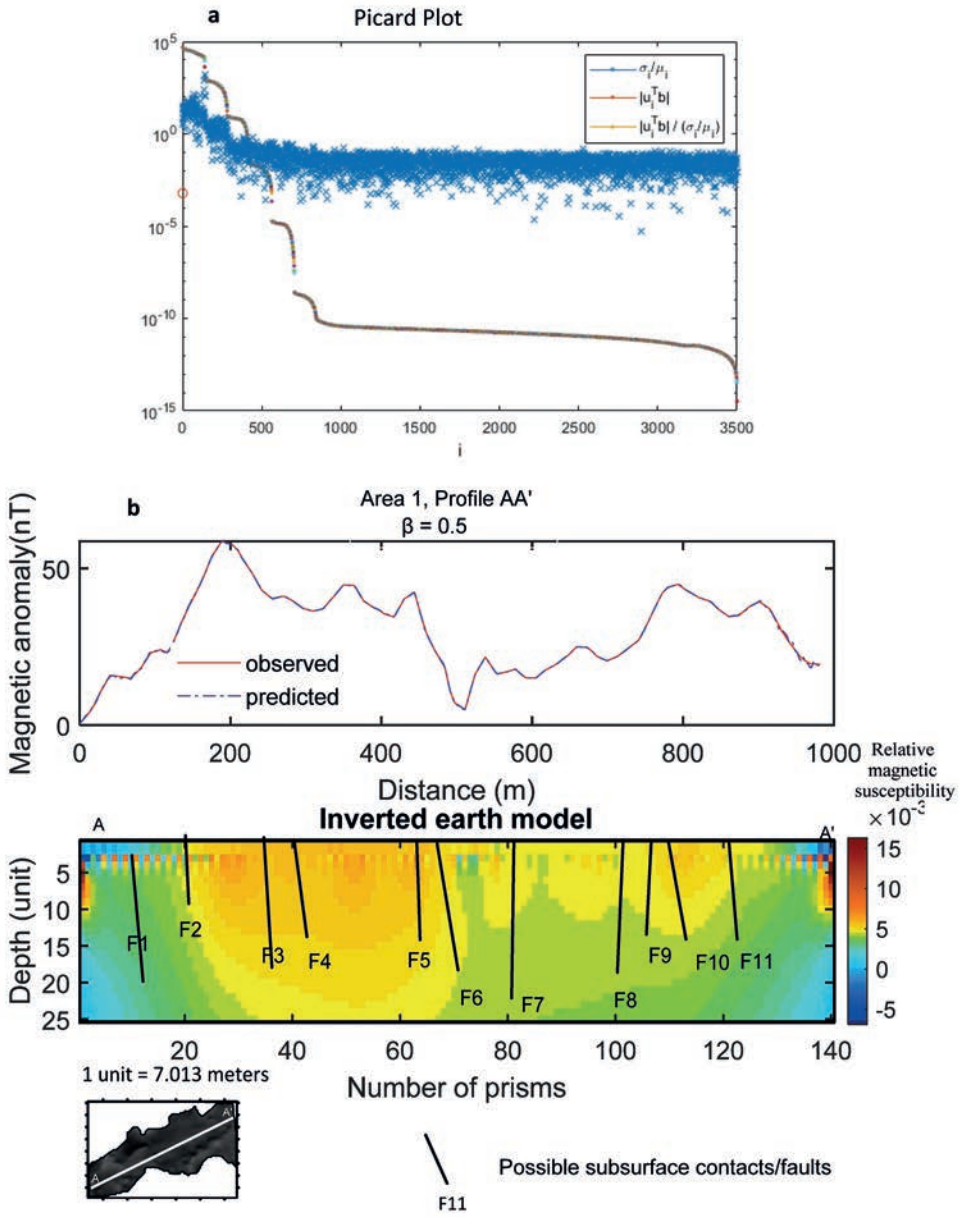

Fig. 13 - Magnetic inversion along profile AA', Area 1 using Kaczmarz (1937) regularisation (Abdelazeem and Gobashy, 2016): a) Picard plot of model, and b) inversion of the measured profile showing distribution of relative magnetic susceptibilities of rock units in the study area with possible contacts/faults indicated with black solid lines. F's indicate the contact/fault number. The depth weighting-function exponent (β) is taken = 0.5.

where α is the regularisation parameter, x_α is the regularised solution, and $A \in \Re^{m\times n}$, $b \in \Re^m$, $\alpha>0$.

Based on the modifications on the above formulation proposed by Ivanov and Zhdanov (2013) and its revised version (Vasil'chenko and Svetlakov, 1980), the system in Eq. 11 is transformed to an augmented system of a linear equation (Zhdanov, 2012) which is always consistent and determined for $\alpha>0$. Now, this is known as the randomised Kaczmarz (1937) algorithm (Strohmer and Vershynin, 2009) and is expressed as:

$$\begin{pmatrix} \omega I_m & A \\ A^T & -\omega I_n \end{pmatrix} \begin{pmatrix} y \\ x \end{pmatrix} = \begin{pmatrix} b \\ 0 \end{pmatrix} \Leftrightarrow \tilde{A}_\omega z = b \tag{12}$$

where $\omega = \sqrt{\alpha}$ and A_ω is non-singular for $\alpha > 0$ (Zhdanov, 2012). The spectral condition number of the system in Eq. 11 can be calculated as (Ivanov and Zhdanov, 2013):

$$\kappa_2(A^T A + \alpha I_n) = \frac{\sigma_{\max}^2 + \alpha}{\sigma_{\min}^2 + \alpha} \tag{13}$$

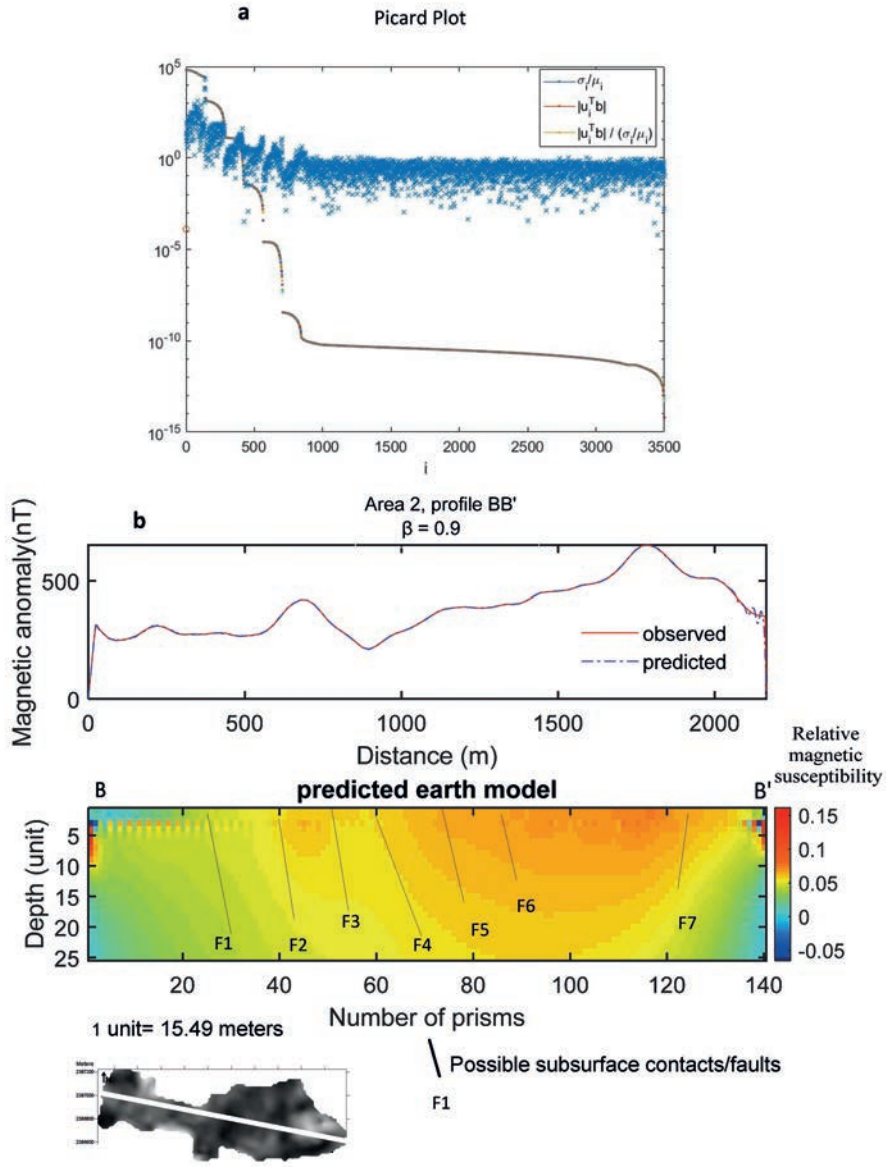

Fig. 14 - Magnetic inversion along profile BB', Area 2 using Kaczmarz (1937) regularisation (Abdelazeem and Gobashy, 2016): a) Picard plot of model, and b) inversion of the measured profile showing distribution of relative magnetic susceptibilities of rock units in the study area with possible contacts/faults posted as black solid lines. F's indicate the contact/fault number. The depth weighting-function exponent (β) is taken = 0.9.

where, σ_{min} and σ_{max} are the minimal and maximal singular numbers of matrix $\boldsymbol{A}$, respectively (singular value decomposition of the kernel $A = U\Sigma V^T$, where $U = (u_1, \ldots, u_n)$ and $V = (v_1, \ldots, v_n)$ are matrices with orthogonal columns, i.e. $U^TU = V^TV = I_n$, and $\Sigma = \text{diag}\,(\sigma_1,\ldots,\sigma_n)$, with elements descending to zero or near zero).

The above used depth weighting diagonal matrix takes the following form:

$$W(m) = 1/(z_m^2 + b_o)^{\beta} \tag{14}$$

Many authors studied the choice of the exponent to the above function. Boulanger and Chouteau (2001) stated that the exponent must lie between 0.5 and 1 and suggested a standard selection of $\beta = 0.8$ or $\beta = 0.9$. Li and Oldenburg (1996) showed that the above depth-weighting function has the form of a power law of z and reflects the fall-off of the field due to block type sources. Numerically, they showed that the function in Eq. 14 approximates the kernel decay directly under the measuring point, if a correct value is assigned to b_o and when z is the observation height and b_o is a parameter empirically chosen by matching the function $W(m)$ with the field produced at an observation point by a column of cells.

The exponent β plays a major role to correctly estimate the depth to the causative body, because it measures the field decay of the source. Li and Oldenburg (1996) suggested using β=3 (in the magnetic case) because, a cubic-shaped cell acts like a dipole source and the magnetic field decays by inverse distance cubed. However, Cella and Fedi (2012) and Paoletti *et al*. (2013) showed that a more consistent choice of β must depend on the field decay of the whole source, i.e. on the field decay of a block ensemble and hence, the most reliable value for β is N (the SI). The SI has to be estimated before the inversion (e.g. by Euler deconvolution).

Application of the above Kaczmarz (1937) regularisation to solve the ill-posed magnetic problem of Wadi Bani Malik requires a proper construction of the subsurface model. In our case, the subsurface model is composed of a 25×140 (Area 1, 1 unit = 7.013 m) and 25×140 cell (Area 2, 1 unit = 15.49 m), which is dependent only on the required resolution. Each cell represents an unknown magnetic susceptibility value at its centre. Running out such an inversion procedure results in a profile showing subsurface variation in magnetic susceptibility with depth. Possible location of contacts and discontinuity in rock units can be simply extracted. Figs. 13 and 14 show the results of this analysis. In Figs. 13a and 14a, the Picard plots for both models are presented to show the poorly posed nature of the problem (Fedi *et al*., 2005). As the minimum of the singular matrix reaches zero, or of the order 10^{-15} (Hansen, 1990) (in our case: $\sigma_{min} = 2.0802 \cdot 10^{-15}$), the division by zero has to be avoided. In other words, the calculated values are the generalised singular values not the simple singular values. So, the plotted values are (σ_i/μ_i) instead of σ_i, $|u^T b|$ and $[|u^T b| / (\sigma_i/\mu_i)]$ instead of $(|u^T b| / \sigma_i)$. The Picard plots for both areas show the high ill-posedness of the problem, which was expected when calculating the condition number above.

In Figs. 13b and 14b, the observed and predicted data are displayed. In both cases, profiles AA' and BB', a complete overlap is obtained in the data window. An interesting correlation between the detected vertical magnetic contacts estimated from the tilt gradient analysis and the Kaczmarz (1937) regularisation solution can be observed along profiles AA' and BB'.

We tested the best choice for β, where we checked different depth weighting function exponents β (close to the SI as inferred from the 3D Euler deconvolution) in order to improve depth resolution of the inversion model. For Area 1, exponent $\beta = 0.1, 0.2, 0.3, 0.4$, and 0.5 are

tested. For Area 2 exponent $\beta = 0, 0.1, 0.2, 0.3, 0.4 \ldots 1$ are used. In conclusion, no recognisable change can be observed at shallow parts of the model. However, we chose to include model with β=0.5 for profile AA' in Area 1, and model with β=0.9 for profile BB' of Area 2 as the best possible choices and at the same time close to the SI abstained by Euler method.

The inversion confirms the cross-Wadi shallow faults F1 to F11 (Area 1) and F1 to F6 (Area 2). These faults control the groundwater flow from the upstream to downstream. Some noisy signals can be observed especially in profile AA' inverted model, because the algorithm is forced to fit minor high frequency variations in the observed data. A possible near surface heterogeneity may also exist, especially because the profile runs along the Wadi, where water could flush the surface/near surface rocks and produce inhomogeneous lithology. This will also affect the near surface magnetic susceptibilities and shift the scale to an apparently higher susceptibility than normal.

5. Discussion and conclusions

We have derived depths and addressed the location of the magnetic sources, especially faults and vertical contacts in Wadi Bani Malik in Makkah. The problem of possible contamination of the groundwater aquifer with the reserved surface sewage water is mainly attributed to the water exchange along the weak fracture zones, faults or vertical magnetic contacts that are dominant in the area and across the Wadi. The locations and lengths of the linear/nonlinear trends dominant in the area are confirmed by trends estimated from many applied filters on the TMI, RTP, NSS, and total gradient anomaly maps. Area 1 is mainly affected by NE-SW (across the Wadi), and E-W (along the Wadi) trending faults, while for Area 2 common fault trends are NW-SE, and NNE-SSW. The remarkable linear and curvilinear trends running NE-SW, and NNE-SSW in both areas are shown in the total gradient maps. These findings agree with the surface faults as marked on Fig. 3 (Moore and Al-Rehaili, 1989).

The analysis of remnant magnetisation in the study areas using Helbig (1963) technique shows that the Q ratio is around 1, and this assumes that the average remnant content in the area is relatively low and continuous analysis of the data, assuming that the magnetisation vector is nearly parallel to the induced field, is still acceptable.

The Euler deconvolution revealing the depth to magnetic causative sources is generally shallow and ranges from 7.44 m (Cluster 4) to 28.96 m (Cluster 2) in Area 1 (tables 1 and 2). Further assessment of the data on clusters 1, 2 and 3 indicate the relatively deep sources, while the depths of clusters 4 and 5 are relatively very shallow. In Area 2, about 7 out of the 9 cluster solutions are contained within the Wadi stream (tables 3 and 4). The tilt gradient method is applied to determine the location of the contacts (zero contour line) and to estimate depths to sources. The resulting maps show that the area is dissected by a system of faults/vertical magnetic contacts (mainly basement rocks) that structurally control the flow of water along the Wadi Bani Malik. Magnetic inversion using Kaczmarz (1937) regularisation to explore variations of rock magnetic susceptibilities was carried out along two profiles running along the Wadi to detect and confirm these faults. A remarkable agreement with the previous results from other filters with the magnetic tomography results confirms these shallow faults/vertical contacts. These magnetic contacts can be effective as a structural barrier and a weak zone along which surface contaminant water may

exchange with the clean groundwater aquifer. Based on these study findings, the drainage system is mainly structurally controlled and the inferred structural trends should be given consideration in any future development in the study area or similar regions.

Acknowledgements. The authors sincerely thank the associate editor Valeria Paoletti and the anonymous reviewers for their thorough reviews, comments and suggestions that significantly helped to improve the earlier version of the paper.

REFERENCES

Abdelazeem M.; 2013: *Regularizing ill-posed magnetic problems using a parameterized trust-region sub-problem*. Contribut. Geophys. Geod., **43**, 99-123.

Abdelazeem M. and Gobashy M.; 2016: *A solution to unexploded ordnance detection problem from its magnetic anomaly using Kaczmarz regularization*. Interpretation, **4**, SH61-SH69.

Adagunodo T.A. and Sunmonu L.A.; 2012: *Ground magnetic survey to investigate on the fault pattern of industrial estate Ogbomoso, southwestern Nigeria*. Adv. Appl. Sci. Res., **3**, 3142-3149.

Al-Garni M.A. and Gobashy M.M.; 2010: *Ground magnetic investigation of subsurface structures affecting Wadi Thuwal area, KSA*. J. King Abdulaziz Univ. - Earth Sci., **21**, 167-193, doi: 10.4197/ear.21-2.7.

Azeem M.A., Mekkawi M. and Gobashy M.; 2014: *Subsurface structures using a new integrated geophysical analysis, south Aswan, Egypt*. Arabian J. Geosci., **7**, 5141-5157.

Beiki M., Clark D.A., Austin J.R. and Foss C.A.; 2012: *Estimating source location using normalized magnetic source strength calculated from magnetic gradient tensor data*. Geophys., **77**, J23-J37.

Blakely R.J.; 1995: *Potential theory in gravity and magnetic applications*. Cambridge University Press, UK.

Boulanger O. and Chouteau M.; 2001: *Constraints in 3D gravity inversion*. Geophys. Prospect., **49**, 265-280, doi: 10.1046/j.1365-2478.2001.00254.x.

Cella F. and Fedi M.; 2012: *Inversion of potential field data using the structural index as weighting function rate decay*. Geophys. Prospect., **60**, 313-336.

Clark D.A.; 2009: *Improved methods for interpreting magnetic gradient tensor data*. In: Proc. Scientific Assembly, International Association of Geomagnetism and Aeronomy IAGA 11, Sopron, Hungary, p. 1212.

Cordell L. and Grauch V.J.S.; 1985: *Mapping basement magnetization zones from aeromagnetic data in the San Juan basin, New Mexico*. In: Hinze W.J. (ed), The utility of regional gravity and magnetic anomaly maps, Society of Exploration Geophysicists, pp. 181-197, doi: 10.1190/1.0931830346.ch16.

Doll W., Gamey T., Beard L., Bell D. and Holladay J.; 2003: *Recent advances in airborne survey technology yield performance approaching ground-based surveys*. The Leading Edge, **22**, 420-425.

Ewea H.; 2010: *Hydrological analysis of flooding wastewater lake in Jeddah, Saudi Arabia*. J. King Abdulaziz Univ. - Met. Env. & Arid Land Agric. faculty, **21**, 125-144, doi: 10.4197/met.21-1.9.

Fedi M., Hansen P.C. and Paoletti V.; 2005: *Analysis of depth resolution in potential-field inversion, Tutorial*. Geophys., **70**, A1-A11.

FitzGerald D., Reid A. and McInerney P.; 2004: *New discrimination techniques for Euler deconvolution*. Comput. Geosci., **30**, 461-469.

Gerovska D. and Araúzo-Bravo M.J.; 2003: *Automatic interpretation of magnetic data based on Euler deconvolution with unprescribed structural index*. Comput. Geosci., **29**, 949-960.

Gettings M.E. and Andreasen G.E.; 1983: *An interpretation of gravity andaeromagnetic surveys of the greater Jiddah area, Kingdom of Saudi Arabia*. Saudi Arabian Deputy Ministry for Mineral Resources, Open-File Report USGS-OF-03-31, 37 pp.

Gobashy M.M. and Al-Garni M.A.; 2008: *High resolution Ground Magnetic Survey (HRGM) for determining the optimum location of subsurface dam in Wadi Nu'man, Makkah Al Mukarammah, KSA*. J. King Abdulaziz Univ. - Earth Sci., **19**, 57-83.

Grauch V., Hudson M.R. and Minor S.A.; 2001: *Aeromagnetic expression of faults that offset basin fill, Albuquerque basin, New Mexico*. Geophys., **66**, 707-720.

Hansen P.C.; 1990: *The discrete Picard condition for discrete ill-posed problems*. BIT, **30**, 658-672, doi: 10.1007/BF01933214.

Helbig K.; 1963: *Some integrals of magnetic anomalies and their relation to the parameters of the disturbing body*. Zeitschrift fur Geophys., **29**, 83-96.

Hood P.; 2007: *History of aeromagnetic surveying in Canada*. The Leading Edge, **26**, 1384-1392.

Howell L.E.; 2010: *Characterizing shallow intrasedimentary faults using magnetic depth estimation methods: preliminary results of a high-resolution aeromagnetic survey at the San Luis basin, south-central Colorado*. Senior Integrative Exercise, Advisor: Cameron Davidson, Department of Geology, Carleton College, Northfield, MN, USA, 39 pp.

Ivanov A.A. and Zhdanov A.I.; 2013: *Kaczmarz algorithm for Tikhonov regularization problem*. Applied Mathematics E-Notes, **13**, 270-276.

Kaczmarz S.; 1937: *Approximate solution of systems of linear equations*. Int. J. Contr., **57**, 355-357.

Karavul C., Dedebali Z., Keskinsezer A., Beyhan G. and Demirkol A.; 2010: *Magnetic and electrical resistivity image survey in a buried adramytteion ancient city in western Anatolia, Turkey*. Int. J. Phys. Sci., **5**, 876-883.

Kayode J., Nyabese P. and Adelusi A.; 2010: *Ground magnetic study of Ilesa east, southwestern Nigeria*. Afr. J. Environ. Sci. Tech., **4**, 122-131, doi: 10.5897/AJEST09.220.

Kearey P., Brooks M. and Hill I.; 2013: *An introduction to geophysical exploration, 3rd ed*. John Wiley & Sons, New York, NY, USA, 272 pp.

Lee M.D., Morris W.A. and Ugalde H.A.; 2010: *Mapping of apparent magnetic susceptibility and the identification of fractures: a case study from the Eye-Dashwa lakes pluton, Atikokan, Ontario*. Geophys., **75**, B147-B156.

Li X.; 2006: *Understanding 3D analytic signal amplitude*. Geophys., **71**, L13-L16.

Li Y. and Oldenburg D.W.; 1996: *3D inversion of magnetic data*. Geophys., **61**, 398-408.

Loera H.L., Leal J.A.R., Harris P.D., Gaytan D.E.T., Ruiz V.J.M. and Gogichaishvili A.; 2015: *Geophysical exploration of fractured-media aquifers at the Mexican Mesa central: Satellite City, San Luis Potosí, Mexico*. Surv. Geophys., **36**, 167-184.

Mariita N.O.; 2010: *Application of geophysical methods to geothermal energy exploration in Kenya*. Short Course V on Exploration for Geothermal Resources, organized by UNU-GTP, GDC and KenGen, at Lake Bogoria and Lake Naivasha, Kenya.

Merghelani H.M. and Kinkar A.R.; 1983: *Seismicity studies in Saudi Arabia; recent microearthquakes in the Jiddah area*. Saudi Arabian Deputy Ministry for Mineral Resources, Open-File Report DGMR-OF-03-21, 169 pp.

Moore T. and Al-Rehaili M.; 1989: *Geologic map of the Makkah quadrangle*. Sheet 21D, Kingdom of Saudi Arabia: DGMR, Geoscience Map GM-107C, 1:250,000 Scale, Ministry of Petroleum and Mineral Resources, Deputy Ministry for Mineral Resources Publication, Jeddah, SA.

Ndatuwong L.G. and Yadav G.S.; 2014: *Identifications of fractured zones in part of hard rock area of Sonebhadra District, UP, India using integrated surface geophysical method for groundwater exploration*. Arabian J. Geosci., **7**, 1781-1789.

Okazaki K., Mogi T., Utsugi M., Ito Y., Kunishima H., Yamazaki T., Takahashi Y., Hashimoto T., Ymamaya Y., Ito H. and Kaieda H.; 2011: *Airborne electromagnetic and magnetic surveys for long tunnel construction design*. Physics and Chemistry of the Earth, Parts A/B/C, **36**, 1237-1246.

Oruç B.; 2011: *Enhancement of linear features from gravity anomalies by using curvature gradient tensor matrix*. In: Proc. 6th Congress of Balkan Geophysical Society, Budapest, Hungary, B15.

Paoletti V., Ialongo S., Florio G., Fedi M. and Cella F.; 2013: *Self-constrained inversion of potential fields*. Geophys. J. Int., **195**, 854-869.

Paoletti V., Fedi M., Italiano F., Florio G. and Ialongo S.; 2016: *Inversion of gravity gradient tensor data: does it provide better resolution?* Geophys. J. Int., **205**, 192-202.

Qari M.H. and Sadagah B.H.; 2006: *Satellite imagery and engineering geological studies of a proposed sewage dumping site, Jeddah, Saudi Arabia*. J. King Abdulaziz Univ. - Earth Sci., **17**, 43-67.

Rehman F. and Cheema T.; 2016: *Effects of sewage waste disposal on the groundwater quality and agricultural potential of a floodplain near Jeddah, Saudi Arabia*. Arabian J. Geosci., **9**, 307-316.

Rehman F., Abuelnaga H.S.O., Harbi H.M., Tariq C. and Atef A.H.; 2016: *Using a combined electrical resistivity imaging and induced polarization techniques with the chemical analysis in determining of groundwater pollution at Al Misk Lake, eastern Jeddah, Saudi Arabia*. Arabian J. Geosci., **9**, 286-296, doi: 10.1007/s12517-016-2423-9.

Roest W.R., Verhoef J. and Pilkington M.; 1992: *Magnetic interpretation using the 3-D analytic signal*. Geophys., **57**, 116-125.

Rogers M., Cassidy J. and Dragila M.; 2005: *Ground-based magnetic surveys as a new technique to locate subsurface drainage pipes: a case study*. Appl. Eng. Agric., **21**, 421-426.

Saheel A., Samsudin A.R. and Hamzah U.; 2011: *Mapping of faults in the Libyan Sirte basin by magnetic surveys*. Sains Malaysiana, **40**, 853-864.

Salem A., Williams S., Fairhead J.D., Ravat D. and Smith R.; 2007: *Tilt-depth method: a simple depth estimation method using first-order magnetic derivatives*. The Leading Edge, **26**, 1502-1505.

Salem A., Williams S., Fairhead D., Smith R. and Ravat D.; 2008: *Interpretation of magnetic data using tilt-angle derivatives*. Geophys., **73**, L1-L10.

Sarma B., Verma B. and Satyanarayana S.; 1999: *Magnetic mapping of Majhgawan diamond pipe of central India*. Geophys., **64**, 1735-1739.

Silva J.B.C.; 1986: *Reduction to the pole as an inverse problem and its application to low-latitude anomalies*. Geophys., **51**, 369-382.

Skiba W.J., Tayeb J., Al-Khatieb S.O. and Khallaf H.M.; 1977: *Geology of the Jiddah Makkah area (21°/39°), Kingdom of Saudi Arabia*. Skiba W.J., Saudi Arabian Directorate General of Mineral Resources, 561 pp., unpublished bulletin.

Soupios P. and Ntarlagiannis D.; 2017: *Characterization and monitoring of solid waste disposal sites using geophysical methods: current applications and novel trends*. In: Sengupta D. and Agrahari S. (eds), Modelling Trends in Solid and Hazardous Waste Management, Springer Singapore, pp. 75-103, doi: 10.1007/978-981-10-2410-8_5.

Spencer C.H. and Vincent P.L.; 1984: *Bentonite resource potential and geology of the Cenozoic sediments, Jiddah region*. Saudi Arabian Deputy Ministry for Mineral Resources, Open-File Report BRGM-OF-04-31, 60 pp.

Stavrev P.Y.; 1997: *Euler deconvolution using differential similarity transformations of gravity or magnetic anomalies*. Geophys. Prospect., **45**, 207-246.

Strohmer T. and Vershynin R.; 2009: *A randomized Kaczmarz algorithm with exponential convergence*. Journal of Fourier Analysis and Applications, **15**, 262.

Vasil'Chenko G.P. and Svetlakov A.A.; 1980: *A projection algorithm for solving systems of linear algebraic equations of high dimensionality*. USSR Computational Mathematics and Mathematical Physics, **20**, 1-8.

Wang G., Ma Z., Li R., Song Y., Qu J., Zhang S., Yan C. and Han J.; 2017: *Integration of multi-source and multi-scale datasets for 3D structural modeling for subsurface exploration targeting, Luanchuan Mo-polymetallic district, China*. J. Appl. Geophys., **139**, 269-290.

Zhdanov M.S.; 2012: *Integral transforms in geophysics*. Springer Science & Business Media, 139 pp.

Corresponding author: Faisal Rehman
Department of Earth Sciences, University of Sargodha
Sargodha 40100, Pakistan
Phone: +92 333 4167946; e-mail: faisal.rehman@uos.edu.pk